Structure of Iron to 1 Gbar and 40 000 K

Lars Stixrude

Department of Earth Sciences, University College London, Gower Street, WC1E 6BT, London, United Kingdom

First-principles calculations show that compression-induced electronic transitions produce a rich phase diagram featuring reentrant stability of the fcc phase with an extremum on the fcc to hcp boundary at 23 Mbar and 19 000 K, conditions similar to those expected at the center of super-Earth exoplanets. Transformations of hcp to fcc at 57 Mbar due to $4s$ to $3d$ electron transfer and from fcc to a body-centered structure at 320 Mbar due to hybridization of the $3d$ with the core $3p$ band are experimentally observable along a quasi-isentrope generated by laser-induced ramp compression.

As the fourth most abundant and the heaviest major refractory element in the Universe, iron is expected to be a dominant constituent of the cores of rocky, ice-giant, and gas-giant planets, including exoplanets. The behavior of iron at pressures beyond Earth's center is expected to be very different from the terrestrial regime, because core electrons, tightly bound to the nucleus at normal conditions, are increasingly excited by compression and participate in bonding, where they influence material properties, including phase stability.

The crystal structure of iron in the cores of planets larger than Earth is currently unknown, although such knowledge is important for understanding the generation of planetary magnetic fields. The stable phase of iron is hexagonal close-packed (hcp) from 0.1 to at least 4 Mbar [1]. At very low pressure and low temperature, magnetism stabilizes the body-centered cubic (bcc) structure, while at low pressure and moderate temperature the face-centered cubic (fcc) phase becomes more stable because of the phonon contribution to the free energy. The wide stability field of the hcp phase, encompassing conditions at Earth's center (3.6 Mbar, 6000 K), is well understood and agrees with the expectations of canonical band theory [2]. Recently, the phase stability of iron has been computed up to 50 TPa (500 Mbar) but only at zero temperature [3].

At superterrestrial pressures, one expects canonical band theory to break down, because it assumes that the $3d$ band does not interact strongly with other states, except for hybridization with the $4s$ band, the influence of which can be accounted for in terms of d electron occupation [2]. This picture is valid at low pressure because the $3p$ and other core electrons are so tightly bound to the nucleus that they do not interact with the $3d$ states. At high compression, the energies of the lower angular momentum states ($4s$ and $3p$) rise more rapidly than that of the $3d$ band, leading to electron transfer and hybridization of the core electrons with the valence electrons.

Iron is an ideal system for revealing the influence of core electrons on phase stability: The work done by compression up to 100 Mbar in iron is similar to that of the $3p$ core

electron binding energy (50 eV). The maximum pressure of our study (1 Gbar = 100 TPa) is the approximate limit of normal matter, beyond which deuterium fusion occurs [4], the process that separates the largest planets from the smallest stars (brown dwarfs). The large number of exoplanets discovered with masses much greater than Jupiter [5] means that central pressures approaching 1 Gbar may be typical of planetary iron in the Universe.

We use finite temperature density functional theory to predict the phase diagram of iron up to 1 Gbar and 40 000 K (Fig. 1). Our results are based on the Mermin
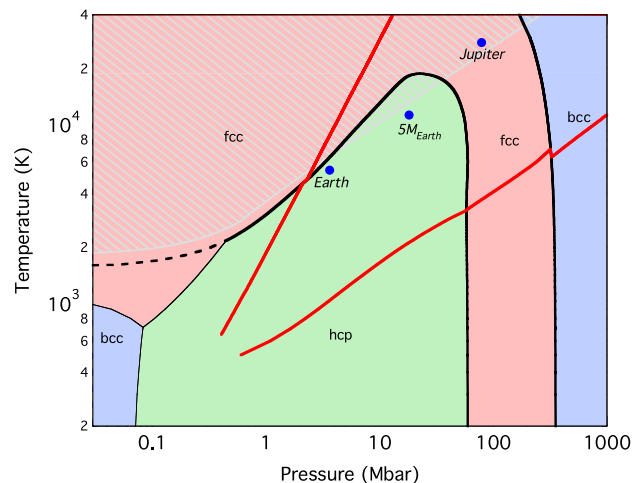

FIG. 1 (color online). Phase diagram of iron. Bold black lines show the results of our calculations including the fcc = hcp and fcc = bcc phase coexistence lines. Thin black lines show the experimental phase boundaries. Superimposed on the phase diagram are (red lines) the calculated isentrope (lower) and Hugoniot (upper). Pressure-temperature conditions at the center of Earth, a super-Earth with 5 times Earth's mass [36], and Jupiter [4] are shown by the blue circles. The calculated fcc = hcp coexistence line is dashed at low pressure where the slope is influenced by magnetic contributions that we have neglected. The stability field of liquid, indicated with gray hatching, is estimated from our computed vibrational frequencies via the Lindemann law [38].

functional [6], which has been applied with success to other systems including iron, where it correctly predicts the stable crystalline phase of iron at conditions of Earth's core [7], and aluminum at higher temperature and pressure [8]. We determine the stable phase at pressure P and temperature T as the one with the lowest Gibbs free energy G. We calculate the Gibbs free energy via the Legendre transformation $G = F + PV$, where F is the Helmholtz free energy, $P = -dF/dV$, and V is the volume [9]. The Helmholtz free energy is $F(V, T) = E_{st}(V) + F_{ph}(V, T) + F_{el}(V, T) + dE_{lat}(V)$, where E_{st} is the static contribution computed at zero Kelvin, F_{ph} is the phonon contribution in the quasiharmonic approximation, and F_{el} is the contribution from the thermal excitation of electrons. The dE_{lat} term is the lattice strain energy due to the slightly nonideal minimum energy value of the c/a ratio in hcp; we assume that dE_{lat} is independent of temperature. We compute all contributions to the free energy in the generalized gradient approximation in the Perdew-Burke-Ernzerhof formulation [10]. Previous studies have shown that the generalized gradient approximation yields excellent agreement with experimental measurements of iron phase equilibria, including the bcc to hcp transition, the stability of hcp at conditions of Earth's core, and the melting curve [7,11,12]. This level of theory is appropriate because the $3d$ bandwidth exceeds the energy of local electronic repulsion (Hubbard U) [13] by more than a factor of 10 in the pressure regime of interest.

We compute the static contributions to the free energy E_{st}, dE_{lat} with the full potential linearized augmented-plane wave with local basis functions method (LAPW + LO) as implemented in the Krakauer-Singh code [14,15], which we used also in our previous study of iron [11], with a $12 \times 12 \times 12$ Monkhorst-Pack k-point mesh [16] and basis set specified by the product of the muffin-tin radius and the maximum momentum $R_{MT}K_{max} = 9.0$. We compute the remaining terms with the projector-augmented plane wave method as implemented in the VASP code [17]. The phonon contribution is computed in the quasiharmonic approximation with help of the code PHON [18] and by using supercells with 64 (bcc), 64 (fcc), and 96 (hcp) atoms, a $4 \times 4 \times 4$ k-point mesh, energy cutoff of 400 eV, and atomic displacements of 1% of the nearest neighbor distance. The phonon and electronic contributions are computed by assuming the Mermin functional of finite temperature density functional theory [6]. All calculations are performed on a dense mesh of volume and temperature points (represented by symbols in the figures) and smoothly and accurately interpolated to obtain the static pressure from the linearized augmented-plane-wave total energy calculations, Gibbs free energies, and phase boundaries.

At low pressure, our results agree well with previous theoretical calculations [19] and with experiment from 1 Mbar up to the maximum pressure explored in static

experiments to date (4 Mbar) [1]. Below 1 Mbar, the slope of the calculated hcp = fcc boundary differs from that experimentally observed because of the influence of magnetism. We have neglected magnetism as in previous high-pressure theoretical calculations [19] because the spin vanishes at $P < 2$ Mbar [20]. We also ignore the liquid phase in this study, as it is stabilized by anharmonic contributions to the free energy that lie beyond the quasiharmonic approximation that we adopt. Continuing the phase diagram into the metastable, supersolidus regime clarifies the origins of crystalline phase stability. We note that anharmonicity may influence the positions of solid-solid phase boundaries. The effect is apparently small for the fcc to hcp boundary: Our quasiharmonic boundary agrees with the fully anharmonic calculation of Ref. [21] to within a few hundred degrees Kelvin near the melting point.

At high pressure, we find reentrant stability of fcc and a body-centered phase at the highest pressures and temperatures (Fig. 1). To understand the predicted phase diagram, we examine the individual contributions to the free energy. The static (low temperature) contribution shows the stabilization of fcc and then bcc over hcp upon compression (Fig. 2). The origin of these phase transitions is found in the band structure (Fig. 3). Within the hcp stability field,
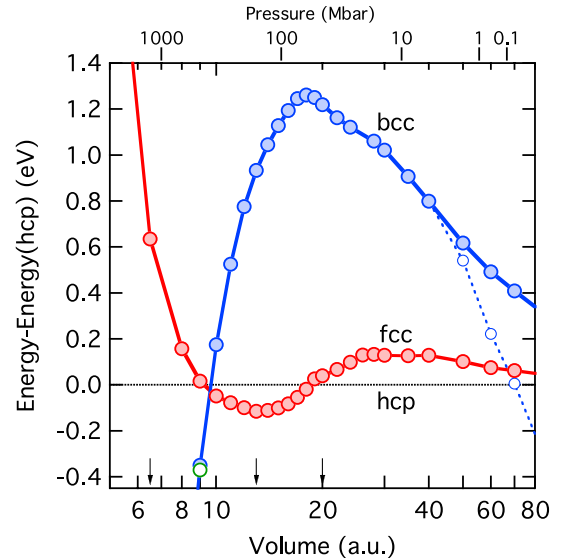

FIG. 2 (color online). Static contribution to the energy: the difference fcc-hcp (red), bcc-hcp (blue), and bct-hcp (green) are shown. Pressure is indicated along the top axis. Downward-pointing arrows indicate the volumes at which band structures are shown in Fig. 3. Properties of phase transformations, including the phase transition pressure P_{tr}, the volume of the low pressure phase V_1, and the volume contrast ΔV are hcp to fcc: $P_{tr} = 60$ Mbar, $V_1 = 18.5$ a.u. (33.9 g/cm^3), $\Delta V = 0.15\%$; fcc to bcc: $P_{tr} = 383$ Mbar, $V_1 = 9.4$ a.u. (66.7 g/cm^3), $\Delta V = 0.1\%$. The dashed blue line and open blue symbols are for ferromagnetic bcc iron from our previous work [11] and show the influence of magnetism on the stability of iron at low pressure.
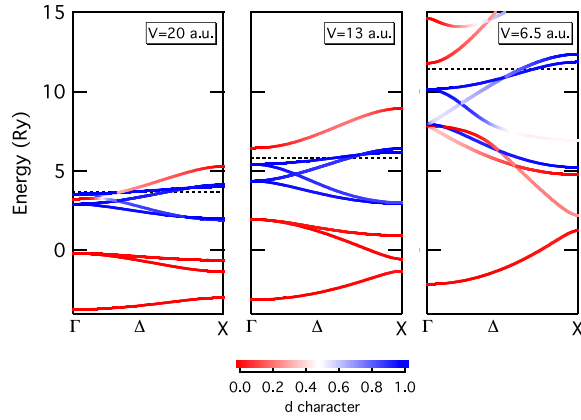
FIG. 3 (color online).   Band structure of iron at high pressure in the stability field of hcp (left), fcc (middle), and bcc (right). The Fermi energy is denoted by the dashed black line. Bands are color-coded according to the amount of d character in the eigenstates as indicated. Bands are well separated in the middle panel in order of increasing energy: $3s$, $3p$, $3d$, and $4s$. Band structures are calculated in the fcc structure.

the band structure of iron is typical of that of $3d$ transition metals at low pressure: The $3d$ band hybridizes with the $4s$ state. Within the fcc stability field, the $4s$ band becomes completely separated from the $3d$ band, causing s to d electron transfer. Within the bcc stability field, the core $3p$ states, which are narrow and tightly bound at low pressure, broaden and hybridize with the $3d$ band. It is possible that other phases of iron are more stable than those we have considered. However, a structural search based on the pseudopotential method at static conditions finds the same sequence of low temperature transitions that we do with an all-electron method and produces no other stable phases up to 500 Mbar, aside from a slight tetragonal distortion of the bcc structure at the highest pressure [3]. We confirm this slight structural distortion, finding that a mechanically stable body-centered tetragonal structure with $c/a = 0.975$ is 20 meV lower in energy than bcc.

Temperature has a large influence on phase stability: The hcp stability field shrinks with increasing temperature, producing reentrant fcc stability (Fig. 1). The origin of the reentrant behavior is seen in the phonon and electronic contributions to the fcc-hcp free energy difference (Fig. 4). These contributions favor fcc over the entire stability field of hcp. The hcp stability field must therefore diminish from low- and high-pressure sides with increasing temperature. The large influence of temperature on stability that we find differs from the conclusion drawn in a previous low temperature study that the influence of temperature would be minor, based on a limited number of calculations of mode frequencies and thermal electronic excitation energies [3]. This discrepancy highlights the importance of fully treating phonon and electronic contributions to the free energy, as we have done.

The phonon and electronic contributions to the fcc-hcp energy difference can be further traced to the vibrational
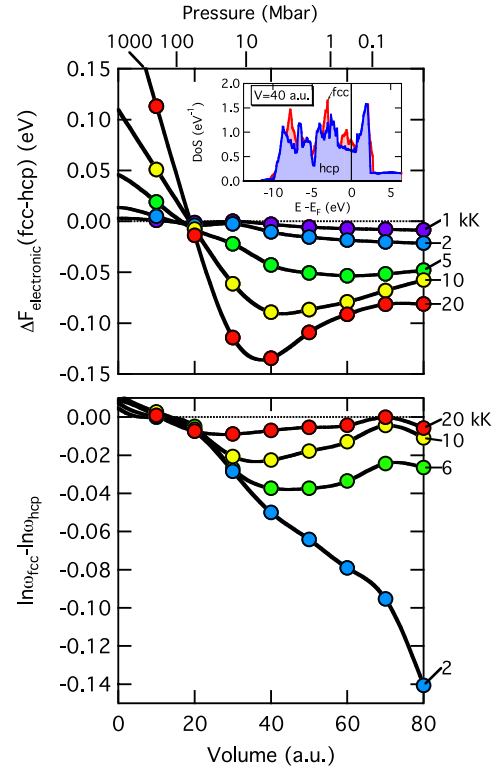

FIG. 4 (color online).   Finite temperature contributions to the free energy including the electronic (top) and phonon (bottom) terms; pressure is indicated along the top axis. The top panel shows the difference in electronic free energy between fcc and hcp phases over a range of temperatures as indicated (1000–20 000 K). The inset shows that the electronic density of states at the Fermi level is higher in fcc than in hcp at high pressure. The bottom panel shows the difference in the logarithm of the geometric mean vibrational frequency, which is directly proportional to the phonon contribution to the free energy.

and electronic densities of states in these structures (Fig. 4). The phonon contribution is more favorable in the case of fcc, because this structure has a lesser mean vibrational frequency (zeroth moment of the vibrational density of states ω_g), which yields $F_{\mathrm{ph}} = kT \ln(\omega_g)$ to within a few meV at high temperature [22,23]. The electronic contribution is more favorable in the case of fcc, because the electronic density of states at the Fermi level $n(E_F)$ is greater. The greater value of $n(E_F)$ in fcc originates in the crystal structure: Different packing sequences $ABCA\ldots$ (fcc) vs $ABAB\ldots$ (hcp) lead to larger hopping contributions to $n(E_F)$ from circuits involving more than two close-packed planes in the case of fcc [24]. This difference in band structure also accounts for the relative instability of fcc as compared with hcp in iron at low temperature [2].

The form of the reentrant fcc → hcp → fcc transition can be understood on the basis of the Claussius-Clapeyron relation $(dT/dP)_{\mathrm{eq}} = \Delta V/\Delta S$, where the subscript indicates the conditions under which the two phases coexist in

equilibrium and ΔV and ΔS are the volume and entropy of transition, respectively. Along the entire hcp $=$ fcc curve, fcc is the higher entropy phase, due to greater phonon and electronic entropies. The fcc phase has larger volume at low pressure, producing a positive Clapeyron slope, and smaller volume at high pressure, producing a negative Clapeyron slope. The two portions of the hcp $=$ fcc boundary of opposite sign converge as temperature increases. At the maximum temperature of hcp stability, the volume of hcp and fcc coincide, producing a vanishing Clapeyron slope. Cobalt also shows a reentrant fcc $\rightarrow$ hcp $\rightarrow$ fcc transition but at much lower pressures [25]. Another important difference with iron is that, in cobalt, magnetism is important in controlling the relative stability of fcc and hcp [26,27].

New experiments, based on laser-driven dynamic compression, have the capability to test our predictions of phase transitions at ultrahigh pressure [28]. In dynamic compression, the temperature rises with increasing pressure. In order to help guide new experiments, we have computed pressure-temperature paths in two limiting cases: shock-wave compression, governed by the Rankine-Hugoniot relation [29] $E - E_0 = (P + P_0)(V - V_0)/2$, where subscripts 0 refer to the preshocked state, and isentropic compression, in which shaped laser pulses produce more gradual compression and, in the limit, no entropy production. In both cases, we have assumed that the precompressed state is ferromagnetic bcc iron at ambient conditions [11].

We find that the temperature along the isentrope rises sufficiently slowly that it crosses the hcp $\rightarrow$ fcc and the fcc $\rightarrow$ bcc transitions (Fig. 1). Along the Hugoniot, in contrast, the temperature rises far too rapidly and enters the supersolidus regime at relatively low pressure. On the isentrope, we predict that the volume and entropy contrasts across the solid-solid phase transitions are small and may not be detectable via measurements of the pressure-density relation alone. Instead, detection of these transitions will likely require the development of *in situ* x-ray diffraction [30] or scattering [31].

We gain additional insight into the origin of the hcp to fcc transition near 50 Mbar, which we attribute to 4s to 3d electron transfer, by relating our results to analyses of phase stability in other transition metals. Canonical band theory predicts that the fcc structure becomes increasingly stable as the d electron occupation increases from Fe to Co to Ni [2]. Our results are compatible with this trend, as increasing the d electron occupation in iron, due to s to d electron transfer, stabilizes the fcc structure on compression (Fig. 3). The influence of s to d electron transfer on phase stability has been studied systematically in the $4d$ transition metals up to 10 Mbar [32]. These calculations also show the tendency for fcc to become increasingly stable with increasing d electron occupation. The transfer of electrons from 4s to 3d bands has also been studied in

nickel, where it is predicted to produce an insulating state at 340–510 Mbar [33]. A previous study of ultrahigh-pressure iron at zero temperature also pointed out that 4s to 3d electron transfer occurred [3] but did not identify this change in the electronic structure as the cause of hcp to fcc transition.

The influence of 3p-3d hybridization on phase stability, which we identify as the origin of the fcc to bcc transition, has been comparatively little explored in transition metal systems. The low temperature transition sequence calculated in Cr and Mo is similar to what we find in iron, with 3p-3d hybridization stabilizing the bcc phase at the highest pressures [34]. Extensions of canonical band theory also show that 3p-3d hybridization tends to stabilize the bcc structure [35].

Our results indicate that solid inner cores of super-Earth exoplanets are composed of iron in the hcp phase (Fig. 1). The crystal structure is significant, because solidification of the inner core from the overlying liquid outer core on cooling is a major driving force for generating planetary magnetic fields [36]. Much of the energy released comes from the exclusion of lighter alloying elements from the inner core as it freezes. At conditions similar to those of Earth's core, it is known that the fcc phase accommodates light alloying elements more readily than hcp [37]. For this reason, the crystalline phase of Earth's core and the amount of energy released on cooling is still uncertain. On the other hand, super-Earth cores lie deeper within the hcp stability field, so that light elements will be more effectively excluded from the growing inner core, contributing to the energy needed for magnetic field generation. Magnetic fields may be a common feature of super-Earth exoplanets, promising a powerful probe of their interior thermal state.

[1] S. Tateno *et al.*, Science **330**, 359 (2010).
[2] H. L. Skriver, Phys. Rev. B **31**, 1909 (1985).
[3] C. J. Pickard and R. J. Needs, J. Phys. Condens. Matter **21**, 452205 (2009).
[4] W. B. Hubbard, A. Burrows, and J. I. Lunine, Annu. Rev. Astron. Astrophys. **40**, 103 (2002).
[5] I. Baraffe, G. Chabrier, and T. Barman, Rep. Prog. Phys. **73**, 016901 (2010).
[6] N. D. Mermin, Phys. Rev. **137**, A1441 (1965).
[7] L. Vocadlo *et al.*, Nature (London) **424**, 536 (2003).
[8] M. P. Desjarlais, J. D. Kress, and L. A. Collins, Phys. Rev. E **66**, 025401(R) (2002).

[9] H. B. Callen, *Thermodynamics* (Wiley, New York, 1960), p. 376.

[10] J. P. Perdew, K. Burke, and M. Ernzerhof, Phys. Rev. Lett. **77**, 3865 (1996).

[11] L. Stixrude, R. E. Cohen, and D. J. Singh, Phys. Rev. B **50**, 6442 (1994).

[12] D. Alfé, G. D. Price, and M. J. Gillan, Phys. Rev. B **65**, 165118 (2002).

[13] M. Cococcioni and S. de Gironcoli, Phys. Rev. B **71**, 035105 (2005).

[14] D. J. Singh, *Planewaves, Pseudopotentials, and the LAPW Method* (Kluwer Academic, Norwall, MA, 1994).

[15] S. H. Wei and H. Krakauer, Phys. Rev. Lett. **55**, 1200 (1985).

[16] H. J. Monkhurst and J. D. Pack, Phys. Rev. B **13**, 5188 (1976).

[17] G. Kresse and D. Joubert, Phys. Rev. B **59**, 1758 (1999).

[18] D. Alfe, Comput. Phys. Commun. **180**, 2622 (2009).

[19] A. S. Mikhaylushkin *et al.*, Phys. Rev. Lett. **99**, 165505 (2007).

[20] G. Steinle-Neumann, L. Stixrude, and R. E. Cohen, Proc. Natl. Acad. Sci. U.S.A. **101**, 33 (2004).

[21] L. Vocadlo *et al.*, Earth Planet. Sci. Lett. **268**, 444 (2008).

[22] T. H. K. Barron, W. T. Berg, and J. A. Morrison, Proc. R. Soc. A **242**, 478 (1957).

[23] D. Alfé, G. D. Price, and M. J. Gillan, Phys. Rev. B **64**, 045123 (2001).

[24] F. Ducastellle and F. Cyrot-Lackmann, J. Phys. Chem. Solids **32**, 285 (1971).

[25] C. S. Yoo *et al.*, Phys. Rev. Lett. **84**, 4132 (2000).

[26] P. Modak *et al.*, Phys. Rev. B **74**, 012103 (2006).

[27] G. Steinle-Neumann, Phys. Rev. B **77**, 104109 (2008).

[28] R. Jeanloz *et al.*, Proc. Natl. Acad. Sci. U.S.A. **104**, 9172 (2007).

[29] H. J. Melosh, *Impact Cratering* (Oxford University, Oxford, 1989), p. 245.

[30] D. H. Kalantar *et al.*, Phys. Rev. Lett. **95**, 075502 (2005).

[31] B. Yaakobi *et al.*, Phys. Rev. Lett. **95**, 075501 (2005).

[32] C. Cazorla, D. Alfe, and M. J. Gillan, Phys. Rev. B **77**, 224103 (2008).

[33] A. K. McMahan and R. C. Albers, Phys. Rev. Lett. **49**, 1198 (1982).

[34] P. Soderlind *et al.*, Phys. Rev. B **49**, 9365 (1994).

[35] R. Ahuja *et al.*, Phys. Rev. B **50**, 14 690 (1994).

[36] C. Tachinami, H. Senshu, and S. Ida, Astrophys. J. **726**, 70 (2011).

[37] A. S. Côté *et al.*, Phys. Earth Planet. Inter. **178**, 2 (2010).

[38] J. J. Gilvarry, Phys. Rev. **102**, 308 (1956).